Article

Influence of cation substitution on the complex structure and luminescent properties of the ZnInO system

Javier García-Fernández, Almudena Torres-Pardo, Javier Bartolomé, Ruth Martínez-Casado, Qing Zhang, Julio Ramírez-Castellanos, Osamu Terasaki, Ana Cremades, and José M. González-Calbet

Chem. Mater., **Just Accepted Manuscript** • DOI: 10.1021/acs.chemmater.0c02038 • Publication Date (Web): 25 Jun 2020

Influence of cation substitution on the complex structure and luminescent properties of the $Zn_kIn_2O_{k+3}$ system

Javier García-Fernández†, Almudena Torres-Pardo†, Javier Bartolomé‡, Ruth Martínez-Casado‡, Qing Zhang§, Julio Ramírez-Castellanos†, Osamu Terasaki§, Ana Cremades‡ and José M. González-Calbet†, #

† Inorganic Chemistry Department, Chemical Sciences Faculty, Universidad Complutense de Madrid, 28040, Madrid, Spain

‡ Materials Physics Department, Physical Sciences Faculty, Universidad Complutense de Madrid, 28040, Madrid, Spain

§ Centre for High-Resolution Electron Microscopy, ShanghaiTech University, Shanghai 201210, China

ICTS National Center for Electron Microscopy, Universidad Complutense de Madrid, 28040, Madrid, Spain

ABSTRACT The effect of In^{3+} substitution by Ga^{3+} or Al^{3+} on the structure and luminescent properties of $Zn_7In_{2-x}M_xO_{10}$ (M=Ga or Al; 0≤x≤1) oxides has been investigated by means of high spatial resolution X-ray spectroscopy and high angle annular dark field images, combined with magic angle spinning nuclear magnetic resonance spectroscopy. Local structural variations have been identified for the Al and Ga-doped samples through the analysis of atomically resolved chemical maps and the identification of their structural environment within the wurtzite lattice. While In^{3+} is distributed in a zig-zag modulation, Al^{3+} and Ga^{3+} are located in a flat distribution at the center of the wurtzite block. Density functional theory calculations provide unambiguous evidence for the preferential flat location of Ga^{3+} and Al^{3+} associated with the different strain introduced in the structure as a result of their ionic radii. The characterization of the photoluminescence response reveals the appearance of new radiative recombination pathways for the doped materials, due to the presence of new defect levels in the band gap of the $Zn_7In_2O_{10}$ structure.

INTRODUCTION

The homologous series $Zn_kIn_2O_{k+3}$ (*k*=integer), known as IZO, belongs to the family of the transparent conductive oxides (TCO). These optoelectronic materials have attracted an increasing interest due to their good and tunable electrical, optical, thermoelectric and photocatalytic properties depending on *k* and their chemical and thermal stability.[1-5] Their complex structure can be described as formed by the ordered intergrowth between InO_2^- layers in octahedral coordination (hereafter referred as In-O) and $InZn_kO_{k+1}^+$ blocks with wurtzite related structure (for the sake of simplicity referred to as In/Zn-O blocks), where Zn^{2+} and In^{3+} occupy tetrahedral and trigonal bipyramidal sites, respectively, [6] Li *et al*,[7] by using selected area electron diffraction (SAED) and high resolution transmission electron microscopy (HRTEM), reported the existence of a structural modulation in this system, consisting of an ordered arrangement of In^{3+} atoms inside the wurtzite blocks following a zig-zag pattern. This arrangement is necessary to compensate the polarity inversion produced at each In-O layer, while minimizing the internal strain produced by the different ionic radii of In^{3+} (0.80 Å in octahedral coordination) and Zn^{2+} (0.60 Å in tetrahedral coordination),[8-10] Figure 1 shows a schematic representation of the structure.

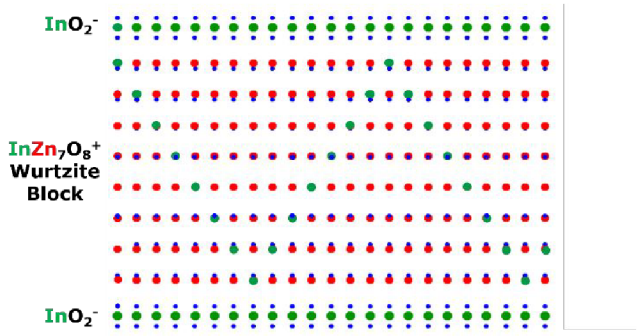

Figure 1. Schematic structural model for $Zn_7In_2O_{10}$ along the $[1\bar{1}0]$ zone axis. Indium, zinc and oxygen atoms are represented in green, red and blue, respectively.

The properties of IZOs can be modified by means of different synthesis strategies, compatible with variations in the cation sublattice composition through chemical doping. The substitution of In by other trivalent cations can substantially modify the electronic structure of the material. This compositional modification not only introduces impurities into the TCO crystal lattice, but also varies the concentration of defects, which can widen the range of optoelectronic applications. For instance, the substitution of In^{3+} by Fe^{3+} or Ga^{3+} gives rise to changes in

the angles and periodicities of the zig-zag patterns.[11-12] However, in the case of Al^{3+} no modulation was observed, so it was supposed to be homogenously distributed inside the wurtzite block.[13] This structural feature and the distribution of these M^{3+} ions inside the $MZn_kO_{k+1}^+$ (M/Zn-O) wurtzite block have been profoundly investigated in the last years by different experimental techniques [9,10] and computational methods.[14,15] A study carried on by Goldstein *et al*,[16] using spherical aberration (Cs) corrected microscopy combined with density functional theory (DFT) calculations on IZO and indium iron zinc oxide (IFZO) nanowires, suggested that the origin of the zig-zag contrast was an inversion of the metal and oxygen positions facilitated by 5-coordinated In or Fe atoms. This model reveals that this defect runs along the {1-21*l*} planes of the wurtzite structure, where the value of *l* depends on the cation (In or Fe).

Other experimental techniques have been used in the study of the IMZO (M= Ga, Al) system. In this sense, Keller *et al*,[17] from single crystal X-ray diffraction and convergent beam electron diffraction (CBED) on Zn_4InGaO_7, found that Ga^{3+} ions are in trigonal bipyramidal (TBP) sites in the wurtzite block, forming an equatorial plane at half distance between the InO_6 octahedral layers to promote the inversion of the wurtzite structure. Narendranath *et al*[18] using Magic Angle Spinning Solid State Nuclear Magnetic Resonance (MAS NMR) of ^{71}Ga and EXAFS, reported that Ga/Zn-O wurtzite blocks are formed by outer strata of ZnO and an inner layer of Ga–O/Zn–O. According to their results, when *k* increases the Ga^{3+} coordination shifts from TBP to tetrahedral, probably because Ga_2O_3 has solubilized in ZnO (especially at high *k* values), and hence, has a wurtzite type structure with corner sharing tetrahedra.

IMZO (with M=Ga, Al) phases stand out due to their interesting properties for many optoelectronic and thermoelectric applications. For instance, Nomura *et al*[19] reported the outstanding carrier transport properties of $InGaO_3(ZnO)_5$ single crystal thin films. Préaud *et al*[20] studied the influence of *k* in the thermal conductivity of the $InGaO_3(ZnO)_k$ homologous series. The values observed for $InGaO_3(ZnO)_3$ are significantly lower than the ones obtained for the binary oxides In_2O_3 and ZnO, and are even lower than the ones observed for the IZO series. Moreover, they found that the band gap monotonically decreases when *k* increases, contrary to the case of IZO compounds.[2,5] Other noteworthy features of this system and, in particular, in the case of $In_{2-x}Ga_xO_3(ZnO)_m$ nanowires, are the improvement of the thermoelectric figure of merit by 2.5 orders of magnitude, in comparison to undoped ZnO nanowires, and the excellent sensitivity to ultraviolet light irradiation as photodetectors.[21-23] In the case of Al^{3+} doping, Košir *et al*[24] reported the improvement of the thermoelectric properties caused by the small addition of Al^{3+} in $Zn_5In_2O_8$ ceramics. On the other hand, only few studies about the influence of In^{3+} substitution in the luminescent properties of IMZOs (M=Ga, Al) performed on microwires have been reported so far.[25,26] Photoluminescence (PL) studies for these materials revealed an intense band around 3.2 eV that could be attributed to near band edge emission and a weak emission band originated by oxygen vacancies. However, in the case of well-ordered single phase ceramics materials, no information has been reported yet. In this sense, it is worth elucidating the effect of the substitution of In^{3+} by Ga^{3+} and Al^{3+}, specially their atomic distribution and the influence in their properties. These properties are strongly dependent on the structure of the selected material, and it has been proposed that the large anisotropy produced by the complex structure of Zn_kInMO_{k+3} oxides can be behind their enhanced performance.[27] Therefore, a deep knowledge of the structure is crucial for the rational optimization of their properties and the search for new applications.

In this paper, the synthesis of Ga^{3+} and Al^{3+} doped $Zn_kIn_2O_{k+3}$ is reported. For a better understanding of the influence of Ga^{3+} and Al^{3+} substitution in the In-(Ga/Al)-Zn-O system, the Zn content, i.e., the *k* value, has been fixed for the composition $Zn_7In_{2-x}M_xO_{10}$ (M=Ga, Al). The structure-luminescent properties relationship has been extensively investigated after a careful chemical and structural characterization. The local structural variations caused by the replacement of In^{3+} by Al^{3+} and Ga^{3+}, have been elucidated from the study of the first chemical environment of the dopants by Magic Angle Spinning Solid State Nuclear Magnetic Resonance (MAS-NMR) as well as from their direct chemical imaging within the wurtzite-type lattice. In this sense, X-ray spectroscopy has been used for the acquisition of atomic chemical maps despite the technical advantages offered by electron energy loss spectroscopy (EELS) mapping because the energy proximity of the Zn-$L_{2,3}$, Ga-$L_{2,3}$ and Al-K lines prevents the precise analysis of the EELS signals. DFT calculations have been performed to confirm the different distribution of the dopants and the PL response of doped materials has been discussed.

EXPERIMENTAL SECTION

Powders of $Zn_7In_{2-x}M_xO_{10}$ (M=Ga, Al with x= 0.25, 0.5, 0.75 and 1.0) were synthesized from ZnO (99.99% Sigma Aldrich), In_2O_3 (99.99% Sigma Aldrich), Ga_2O_3 (99.99% Sigma Aldrich) and Al_2O_3 (99.999% Strem Chemicals). Mixtures of the starting compounds in the stoichiometric ratio were thoroughly ground together in an agate mortar. Raw powders were treated at 1325 °C for 48-56 hours in air. Intermediate grindings every 24 hours were performed until a single phase was reached.

X-ray diffraction (XRD): XRD patterns were recorded using a PanalyticalX'Pert Pro Alpha-1 instrument, equipped with a primary fast X'Celerator detector operating at 45 kV and 40 mA, and fitted with a primary curved Ge (111) monochromator in order to obtain Cu Kα1 radiation (λ = 1.5406 Å). Data were collected at 2θ between 5° and 70°, with a step size of 0.01° and a collection time of 3 s/step. XRD data were analyzed using the software package FullProf

Magic Angle Spinning Solid State Nuclear Magnetic Resonance (MAS- NMR): ^{71}Ga and ^{27}Al solid-state NMR

spectra were recorded with a magnetic field of 9.4 T on a Bruker Avance 400 solid-state spectrometer (corresponding to the ^{27}Al frequency of 104.26 MHz and to ^{71}Ga frequency of 122.02 MHz). The pulse widths were 4.0 μs and 4.5 μs for ^{71}Ga and ^{27}Al, respectively, and the delay time was 5 seconds for both elements. The spinning speed was 12 kHz using 4.0 mm zirconia rotors. Due to the low sensitivity of the ^{71}Ga nucleus, 2000 scans were collected. ^{71}Ga and ^{27}Al spectra´s were referenced with respect to $NH_4Al(SO_4)_2$ and $Ga(NO_3)_3$, respectively.

For electron microscopy observations, the samples thus prepared were crushed in an agate mortar, then ultrasonically dispersed in n-butanol and transferred to carbon coated copper grids. Selected area electron diffraction (SAED) and high-resolution transmission electron microscopy (HRTEM): SAED studies were carried out in a JEOL 2100HT electron microscope and HRTEM was performed in a JEOL JEM 3000F, fitted with a double-tilting goniometer stage (±22°, ±22°). Scanning Transmission Electron Microscopy (STEM): Atomic resolution study was performed on a JEOL JEM-GRANDARM 300F equipped with cold FEG and double Cs correctors operating at 300 kV with a CL aperture of 30 μm, with beam current of 14.7 pA for Ga-doped sample and 31.6 pA for the Al-doped one. High angle annular dark field (HAADF) images were recorded using a nominal camera length of 100 mm and inner and outer collection semi-angles of 64 and 180 mrad, respectively. Bright field images were acquired at the same camera length, with collection semiangle of 15 mrad. Energy dispersive x-ray spectroscopy (EDS) experiments were acquired with two SSD detectors, both with an active area of 100 mm2. HAADF and annular bright field (ABF) images of Zn_7InGaO_{10} along [010], were recorded in a JEOL JEM-ARM 200cF equipped with cold FEG operating at 200 kV using a nominal camera length of 60 mm and inner and outer collection semi-angles of 68 and 280 mrad and 11-22 mrad, respectively.

Density Functional Theory Calculations: All DFT calculations have been performed using the CRYSTAL program,[28] in which the crystalline orbitals are expanded as a linear combination of atom-centered Gaussian orbitals, the basis set. Zn, O, Ga and Al ions are described using all-electron basis sets contracted as s(8) p(64111) d(41), s(8) p(411) d(1), s(8) p(64111) d(41), and s(8) p(621) d(1), respectively. For the In ion an effective core pseudopotential basis set has been used.[29] Electronic exchange and correlation were approximated by using the screened Heyd–Scuseria–Ernzerhof (HSE), which has been shown to correctly describe the fundamental band gaps and electronic structure of oxides.[30,31] In order to meet the required chemical composition, the supercell (8 x 2 x 1) has been considered. Integration over the reciprocal space was carried out using Monkhorst-Pack (MP) meshes of 2 × 2 × 2. The self-consistent field (SCF) algorithm was set to converge at the point at which the change in energy was less than 10–7 Hartree per unit cell. The internal coordinates have been determined by minimization of the total energy within an iterative procedure based on the total energy gradient calculated with respect to the nuclear coordinates. Convergence was determined from the root-mean-square (rms) and the absolute value of the largest component of the forces. The thresholds for the maximum and the rms forces (the maximum and the rms atomic displacements) have been set to 0.00045 and 0.00030 (0.00180 and 0.0012) in atomic units. Geometry optimization was halted when all four conditions were simultaneously satisfied.

Photoluminescence (PL): PL temperature and emission maps were carried out by means of a FLS1000 photoluminescence spectrometer equipped with a 450 W xenon arc lamp as excitation light source. A 395 nm high pass filter was used to eliminate any spurious light coming from the lamp. RT photoluminescence (PL) measurements at different excitation densities were also performed on a Horiba Jobin-Yvon LabRam HR800 confocal microscope with a 325 nm He-Cd laser as excitation source and a neutral filter (optical density 3) to vary the excitation density. All the spectra have been corrected to account for the system response and, in the former case, the emission spectrum of the Xe lamp.

RESULTS AND DISCUSSION

XRD patterns corresponding to the reference material $Zn_7In_2O_{10}$, (hereafter referred as UD, undoped) can be indexed on the basis of a hexagonal unit cell with space group R-3m and refined lattice parameters a=3.31(1) Å and c=73.62(3) Å. All samples with composition $Zn_7In_{2-x}M_xO_{10}$ ($0 \le x \le 1$) were obtained as single phases (SI Figure SI1a-b). From the XRD profiles, it can be observed that lattice parameters decrease as the Ga^{3+} and Al^{3+} content increases (Table I), due to their smaller ionic radii.[8] It is worth emphasizing that the maximum amount of Ga or Al that can be introduced is x=1. The addition of more Ga_2O_3 or Al_2O_3 provokes the appearance of disordered intergrowths or secondary phases such as the $ZnAl_2O_4$ spinel. According to these results, it can be concluded that a solid solution $Zn_7In_{2-x}M_xO_{10}$ (M=Ga, Al; $0 \le x \le 1$) has been stabilized.

Table I. Cell parameters *a* and *c* for $Zn_7In_{2-x}M_xO_{10}$ (M=Ga, Al).

x value	Ga^{3+}		Al^{3+}	
	a (Å)	*c* (Å)	*a* (Å)	*c* (Å)
0.25	3.31(1)	73.42(3)	3.30(1)	73.38(3)
0.50	3.30(1)	73.27(3)	3.28(1)	73.11(3)
0.75	3.29(1)	72.99(5)	3.27(1)	72.79(6)
1.0	3.28(1)	72.71(6)	3.26(1)	72.47(6)

Figures 2a-d show the SAED patterns corresponding to $Zn_7In_2O_{10}$, Zn_7InGaO_{10} and Zn_7InAlO_{10} along the $[1\bar{1}0]$ zone axis, respectively. The reflection conditions are consistent with the space group R-3m. As mentioned above, Li *et al* reported[7, 11-13] the existence of a structural modulation, which clearly manifests as satellite spots that become more intense for the higher members of the series. In $Zn_7In_2O_{10}$, these sharp satellite spots are clearly visible (indicated with yellow arrows in Figure 2a and displayed in the enlarged

image in Figure 2b). However, in substituted samples the intensity of these reflections gradually decreases as the M^{3+} content increases until they disappear for x=1.0. Additionally, the well-defined diffraction spots observed indicate the high crystallinity of the material as shown in the corresponding HRTEM images, where the formation and stabilization of the superstructure between the In-O and M/Zn-O blocks is identified (SI Figure SI2).

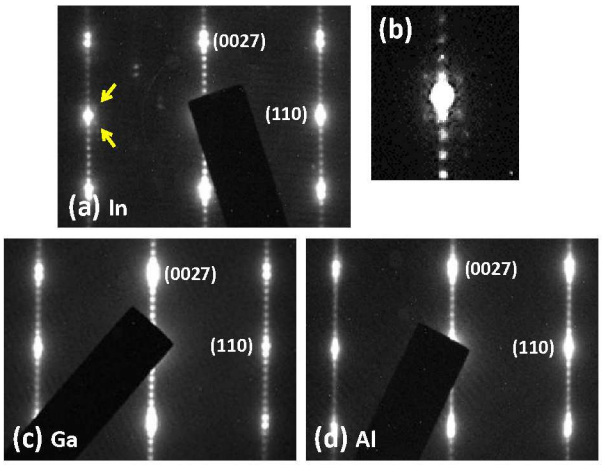

Figure 2. SAED pattern acquired along the [1$\bar{1}$0] zone axis of (a) $Zn_7In_2O_{10}$, Satellite spots are pointed by yellow arrows. (b) Corresponding enhanced SAED around the (110) reflections. SAED patterns of (c) Zn_7InGaO_{10} and (d) Zn_7InAlO_{10}.

A representative high angle annular dark field (HAADF) image of $Zn_7In_2O_{10}$ along [1$\bar{1}$0] is shown in Figure 3a. The location of the indium atoms is clearly visible as the brighter contrast (Z=49) in the In-O layers and inside the In/Zn-O wurtzite blocks following a zig-zag pattern (marked as dashed green lines for a better visualization). Previous reports in $Zn_kIn_2O_{k+3}$ confirm the existence of this structural modulation in all the homologous series,[4,7,9-12] which is caused by a non-homogenous distribution of In^{3+} in trigonal bipyramidal sites following a zig-zag pattern. Darker contrast is observed from the atomic columns corresponding to Zn (Z= 30) only in the wurtzite blocks. A high resolution HAADF image is shown in Figure 3b. In this image, a subtle displacement of the metallic ion along the *c* axis when crossing the zig-zag layer is observed (marked as dashed orange line). This displacement is the result of a change in the orientation of the ZnO_4 tetrahedra at both sides of the zig-zag layers. This situation has been visualized before by Cs corrected HRTEM and STEM[32] and supported by DFT calculations.[16] Moreover, Figure 3c shows the corresponding BF image where the zig-zag modulation, observed in this case as dark shadows, is clearly distinguished in the In/ZnO blocks. This contrast in the BF image is related to the presence of a strain field inside the blocks caused by the presence of In^{3+} in the wurtzite matrix. Yu *et al*[33] studied the strain field in $Zn_kIn_2O_{k+3}$. According to their results, the main strain component on *ab* plane provides evidence for dilatations concentrated at zig-zag layers, while the wurtzite blocks remain unstrained.

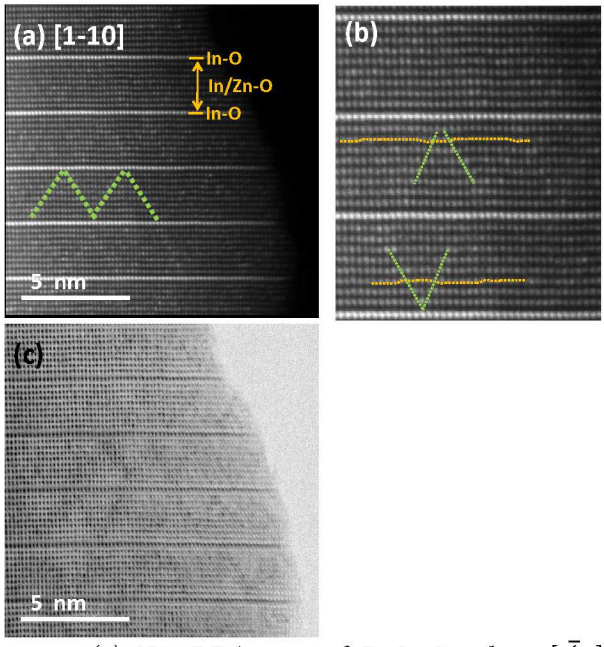

Figure 3. (a) HAADF images of $Zn_7In_2O_{10}$ along [1$\bar{1}$0]. Dashed green lines indicate the zig-zag modulation. (b) High resolution HAADF image of (a). Dashed orange lines indicate the shift in the metal sublattice. (c) BF image along the same zone axis. Zig-zag modulation is observed in all images.

The microstructural characterization of doped Zn_7InGaO_{10} by combining HAADF and ABF images with atomic resolution along [010] allowed locating, as expected, the inversion of polarity due to the gradual change in the position of O atomic columns along [001] (SI Figure SI3). Figures 4a-b show the HAADF and BF images of the same sample along [1$\bar{1}$0]. The location of the In^{3+} atoms is clearly visible as the brighter contrast in the In-O layers, while darker contrast is observed from the columns of atoms corresponding to Zn (Z= 30) and Ga (Z= 31) in the wurtzite blocks. It is important to notice that neither the HAADF nor the BF images show any zig-zag pattern caused by a possible ordered distribution of Ga cations inside the Ga/Zn-O blocks. Instead, a very homogenous contrast inside the wurtzite blocks is observed, due to the similar atomic number between Ga and Zn preventing their location from the contrast of the HAADF image.

In order to clarify any possible cationic ordering in the Ga/Zn-O blocks, the distribution of In, Ga and Zn in Zn_7InGaO_{10} was investigated by atomically resolved STEM-EDS mappings in the area of interest, marked with a yellow rectangle, in the HAADF image. The chemical map from In-L_α confirms the absence of In^{3+} inside the wurtzite block, showing that it is only located in the In-O layer (Figure 4c). Chemical maps from Zn-K_α and Ga-K_α (Figures 4d-e) reveal that both elements are located inside the wurtzite blocks, with the Ga^{3+} located at the middle and without evidence of any zig-zag ordering, as expected from the absence of satellite spots in the SAED study. Figure 4f

shows the composed image of the three elements where the flat

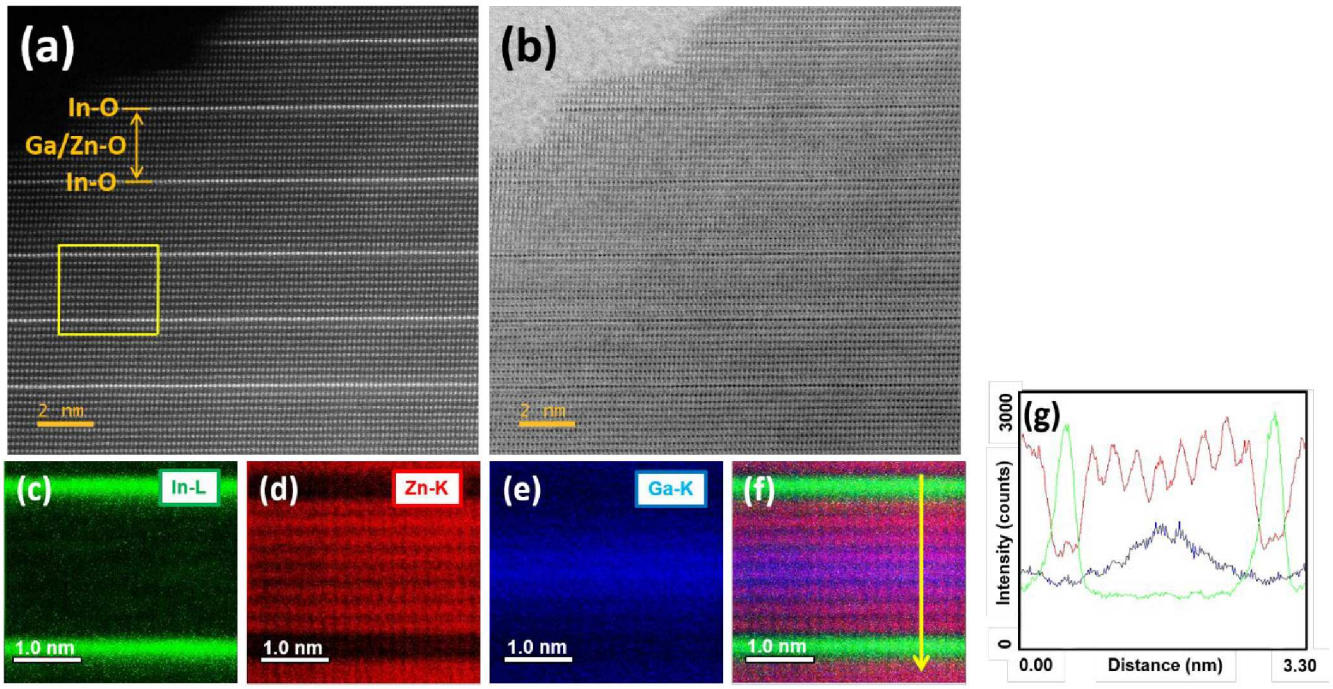

Figure 4. (a) HAADF and (b) BF images along [$1\bar{1}0$] of Zn_7InGaO_{10} and corresponding EDS elemental maps: (c) In-L_α (green), (d) Zn-K_α (red), (e) Ga-K_α (blue) and (f) overlapping. (g) Signal profiles of the different elements obtained from EDS.

disposition of Ga^{3+} at the center of the wurtzite block is unambiguously revealed. Figure 4g shows an intensity profile of the three elements along the yellow arrow depicted in Figure 4f. From this profile, an increase in the Ga concentration towards the middle of the block is confirmed, correlated with the corresponding decrease of the Zn signal. These atomic maps show for the first time, a direct interpretable image of the cationic distribution in the In-Ga-Zn-O system that was previously described by Keller *et al*[17] and Narendranath *et al*[18]

In the case of Al^{3+}, Figure 5a shows a typical HAADF image of Zn_7InAlO_{10} along [$1\bar{1}0$]. In this case, again, we can observe the In-O layers corresponding to the brightest contrast and the lacking of the zig-zag modulation in the wurtzite block, in good agreement with the absence of satellite spots in the SAED study. In addition, inside the Al/Zn-O blocks, a darker disordered contrast in the middle of the block is seen, suggesting the presence of Al^{3+} (Z=13) in the central area of the wurtzite-block. Effectively, the chemical mappings using EDS lines from In-L_α, Zn-K_α, Al-K_α and the sum of all, indicate that Al^{3+} locates in a flat disposition inside the wurtzite blocks, while In^{3+} is only at the In-O layers (Figures 5b-e). The intensity profile across the yellow arrow depicted in Figure 5f confirms this picture,

the Al signal increasing around 2-4 layers at the center of the block, while the Zn signal decreases. Notice that a small presence of Al^{3+} is detected inside the In-O layer (blue circle in Figure 5f), which makes a clear difference with the Ga-doped sample since Ga^{3+} was only detected inside the wurtzite block.

The differences in the structural accommodation of M^{3+} (M= In, Ga, Al) might be influenced by changes in the coordination geometries. Previous studies on Zn_kInGaO_{k+3} show that Ga^{3+} could be occupying a BPT or a Td coordination,[17,18] however, no information about coordination states of Al^{3+} in these phases has been reported. In order to clarify this question, we have employed MAS NMR, which is a powerful tool to understand the local environments of magnetically active nuclei. In our case, ^{71}Ga and ^{27}Al MAS NMR studies were carried out to estimate the coordination number of Ga^{3+} and Al^{3+} in Zn_7InGaO_{10} and Zn_7InAlO_{10}, respectively. From these data, the tetrahedral coordination of Ga^{3+} (signal at 210 ppm, see Figure 6a)[18,34] and Al^{3+} (signal at 75-85 ppm, see Figure 6b) is confirmed. However, a small and broad band in the range 5-15 ppm, which corresponds to Al^{3+} in octahedral site,[35] is also detected, which can be due to the small amount of Al^{3+} in octahedral coordination randomly distributed in the In-O layers.[24]

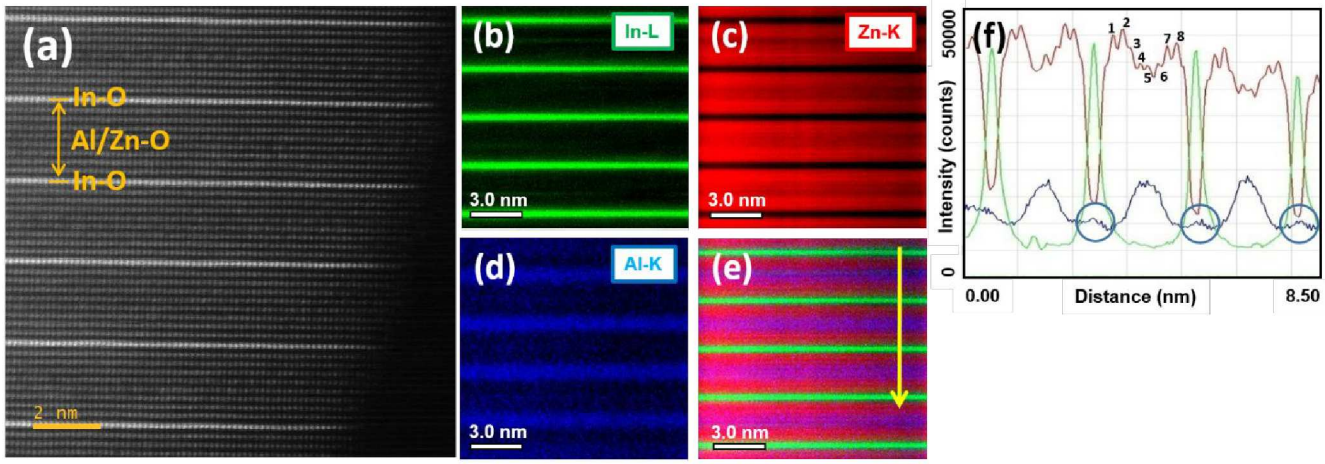

Figure 5. (a) HAADF image of Zn_7InAlO_{10} along [$1\bar{1}0$] and corresponding EDS elemental maps: (b) In-L_α (green), (c) Zn-K_α (red), (d) Al-K_α (blue) and (e) overlapping. (f) Signal profiles of the different elements obtained from EDS. Numbers indicate the wurtzite planes. Blue circles indicate the presence of Al^{3+} in the In-O layer

These data confirm the information obtained from the atomically-resolved EDS maps (Figure 5f), where a small amount of Al^{3+} was detected in the In-O layers. A closer look to the Al^{3+} tetrahedral resonance peak (Al_{IV}) reveals that this maximum is actually a doublet (see inset in Figure S6b). The origin of this doublet and a schematic representation of the Zn/Al distribution is discussed (see SI Figure SI4).

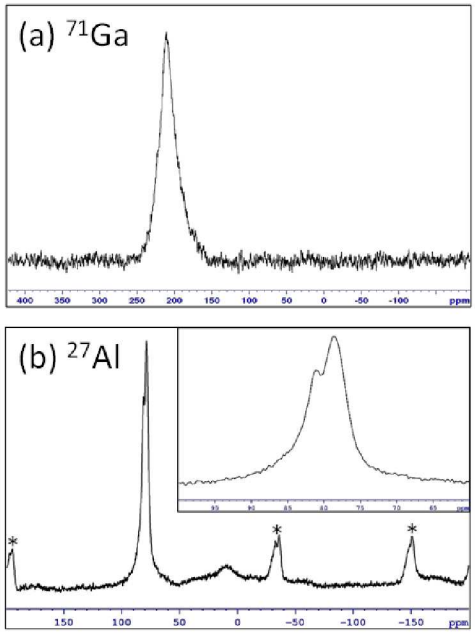

Figure 6. (a) MAS NMR spectra of ^{71}Ga in Zn_7InGaO_{10} and (b) MAS NMR spectra of ^{27}Al in Zn_7InAlO_{10}. Asterisks indicate the spinning sidebands belonging to the tetrahedral resonance. The inset shows an enlargement in the 60-100 ppm range.

Considering all this information, the substitution of In^{3+} by Ga^{3+} or Al^{3+} inside the wurtzite block causes the disappearance of the structural modulation, placing Ga^{3+} and Al^{3+} in the middle of the block in a flat arrangement in tetrahedral coordination. To confirm the stabilization energies of these atomic arrangements, DFT calculations were carried on. A first principles analysis of the $Zn_7In_2O_{10}$, Zn_7InGaO_{10}, and Zn_7InAlO_{10} structures has been performed by using DFT. The excellent agreement obtained in the lattice parameters between DFT and XRD can be seen in Table II, where the inclusion of Ga^{3+} and Al^{3+} leads to a reduction of the unit cell volume. Both modulated in zig-zag (ZZ) and flat (F) positions of the In, Ga or Al atoms inside the wurtzite blocks have been considered. The relative stability has been analyzed by comparing the total energy of the fully relaxed structures (see Table III). As it can be seen, the total energy of the modulated structure is 0.30 eV/f.u. lower than that of the flat one for $Zn_7In_2O_{10}$. However, the flat structure is more stable for 0.10 eV/f.u. when the In^{3+} is substituted by Ga^{3+}, and for 0.25 eV/f.u. when it is substituted by Al^{3+} in the wurtzite blocks. The most stable optimized structures for $Zn_7In_2O_{10}$, Zn_7InGaO_{10}, and Zn_7InAlO_{10} can be seen in Figures 7a-c. It is worth mentioning the good agreement between these structures and the tetrahedral coordination in Al/Ga polyhedral, with the results obtained by MAS NMR and EDS chemical maps presented in Figures 4 and 5. A scheme of all the considered structures is shown in SI Figures SI5-SI6.

Table II. Comparison of the cell parameters obtained by DFT and XRD for Zn_7InMO_{10} (M=In, Ga, Al). The percentage of error of DFT with respect to XRD is shown in parenthesis.

Method	In^{3+}		Ga^{3+}		Al^{3+}	
	a (Å)	*c* (Å)	*a* (Å)	*c* (Å)	*a* (Å)	*c* (Å)
DFT (ZZ)	3.32 (0.3)	73.76 (0.2)	3.28 (0.0)	72.68 (0.0)	3.26 (0.0)	72.68 (0.3)
DFT (F)	3.32 (0.3)	74.22 (0.8)	3.27 (0.3)	73.09 (0.5)	3.26 (0.0)	72.60 (0.2)
XDR	3.31	73.62	3.28	72.71	3.26	72.47

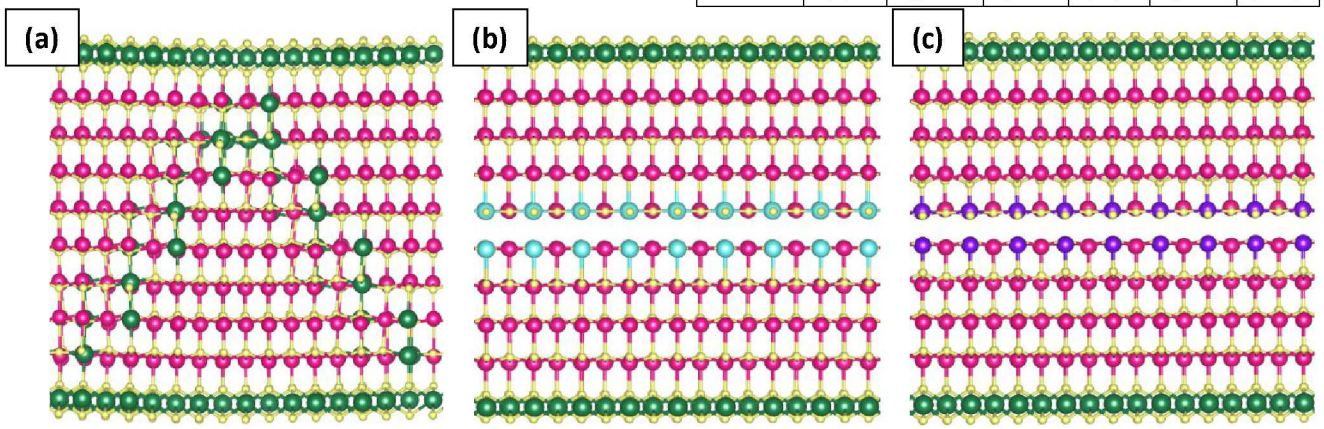

Figure 7. DFT optimized unit cells along the [1$\bar{1}$0] zone axis for (a) $Zn_7In_2O_{10}$, (b) Zn_7InGaO_{10}, and (c) Zn_7InAlO_{10}. Zn, In, Ga, Al, and O ions are represented in pink, green, cyan, purple, and yellow, respectively

DFT calculations on IMZO (M=In, Ga, Al) performed by Yan *et al*[14] and Da Silva *et al*[15] compared the relative energies of the zig-zag model and the flat layer model where M^{3+} ions form a single layer of trigonal bipyramids. Their calculations confirmed the zig-zag modulated structure as the most stable. Nevertheless, their results revealed that the energy difference between the zig-zag configuration and the flat layer decreases from In^{3+} to Al^{3+}, which was explained as a consequence of a reduced strain energy moving from In^{3+} to Al^{3+}. We have performed DFT calculations considering the experimental evidences of flat distribution of Al^{3+} and Ga^{3+} with tetrahedral coordination. In this scenario, DFT predicts the appearance of two flat layers of Ga^{3+} or Al^{3+} in the middle of the block rather than in zig-zag configuration and, in the case of Al^{3+}, a very similar stability can be obtained placing Al^{3+} in four layers as it is experimentally observed (SI Figure SI6 and Table SI1). Another interesting feature of our DFT calculations is the appearance of the inversion of the ZnO_4 tetrahedral across the zig-zag modulation in $Zn_7In_2O_{10}$, in good agreement with our previous HAADF study and with the literature.[16] The fact that DFT shows the appearance of this feature on its own suggests that occurs as a means of reducing the total energy of the system.

Table III. Total energy difference for the relaxed $Zn_7In_2O_{10}$, Zn_7InGaO_{10}, and Zn_7InAlO_{10} structures. Modulated structures have been used as reference.

	In^{3+}	Ga^{3+}	Al^{3+}
$\Delta E = E_{ZZ} - E_F$ (eV/f.u.)	0.30	-0.10	-0.25

To further investigate the luminescent properties of these materials, PL measurements have been carried out at different temperatures, excitation densities and wavelengths. We have focused our study only on those materials with the maximum doping, i.e., with x=1, as well as on the reference undoped (UD) sample. Figure 8a shows the normalized PL spectra of UD ($Zn_7In_2O_{10}$) as a function of the temperature, revealing a wide gaussian band peaked at 1.74 eV. This band has little dependence on the temperature, consisting in a small peak redshift and an asymmetric narrowing of the high energy tail at lower temperatures, suggesting the presence of a second minor band that would have a lower temperature-induced quenching compared to the main band. The existence of this less intense contribution located at around 2.15 eV, is confirmed by two different PL measurements, RT spectra recorded at different excitation densities (see details in SI Figure SI7) and spectra acquired at different excitation wavelengths both at 292 K (RT) and 4 K (see Figures 8(b) and SI8 in the SI). At RT, higher excitation densities or wavelengths lead to an asymmetric broadening of the high-energy tail of the spectra that can be properly explained in all cases by this second contribution. Therefore, the luminescence spectra can be fit to two Gaussian bands centered at $x_{c,1}(In)=1.74 \pm 0.01$ eV and $x_{c,2}(In)=2.15 \pm 0.05$ eV, as it is shown in Figure 8c. While the origin of the 1.74 eV band has been previously established as radiative transitions from singly ionized to doubly ionized Zn vacancies ($V'_{Zn} \rightarrow V''_{Zn}$),[4] the emission center responsible for the 2.15 eV band has not been identified so far. Hopper *et al* performed first principle calculations for both the formation and transition energy levels of different acceptor and donor defects in $Zn_kIn_2O_{k+3}$ (k=3, 5, 7, 9).[36,37] The formation energy of these defects strongly depends on the Fermi level of each compound, however, IZO compounds

tend to present high Fermi levels, close to the conduction band minimum.[38] According to their results, the formation energy of Zn vacancies (V_{Zn}) is the lowest of all acceptor defects at a high Fermi level, and their transition energy level from neutral to singly ionized zinc vacancy ($V_{Zn}^{x} \rightarrow V'_{Zn}$) is at a distance from the conduction band that is closely matched to the energy of the second contribution.

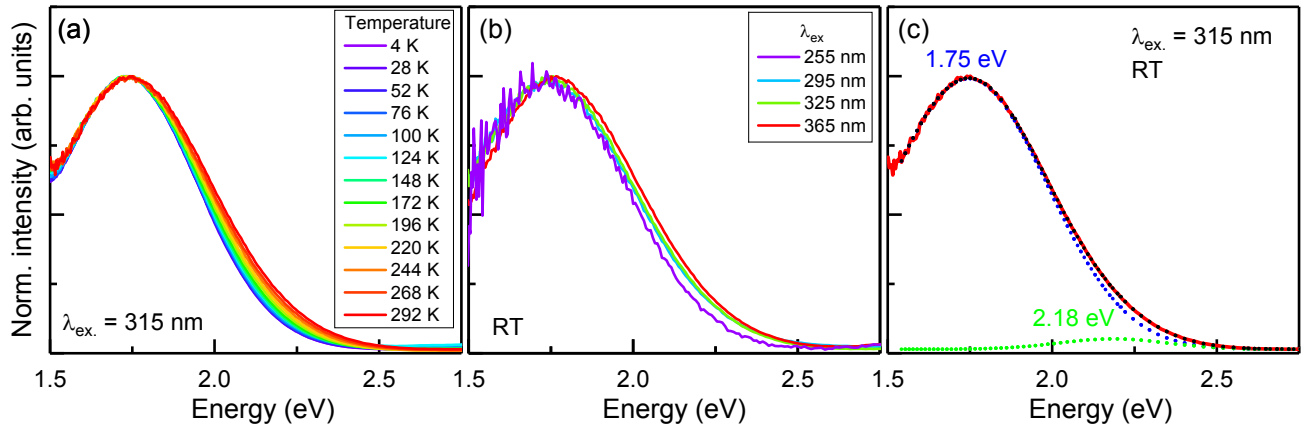

Figure 8. (a) Normalized PL spectra of the undoped sample recorded with an excitation wavelength of 315 nm at different temperatures. (b) Normalized PL spectra obtained at 292 K (RT) at different excitation wavelengths in the range of 255 to 365 nm. (c) Fitted PL spectrum recorded at RT and λ_{ex}=315 nm, showing both bands (blue and green dotted lines) along with their peak center values. Black dotted line corresponds to the sum of both contributions

At high Fermi levels, Zn vacancies tend to be completely ionized.[36] Radiative transitions from singly ionized to doubly ionized Zn vacancies ($V'_{Zn} \rightarrow V''_{Zn}$) -centered at 1.74 eV- presented a decay lifetime below the resolution of our system (50 ns), indicating very fast dynamics for this band. Therefore, the likelihood of exciting both trapped electrons becomes vanishingly small at low temperature and no emission of the $V_{Zn}^{x} \rightarrow V'_{Zn}$ transitions -centered at 2.15 eV- is observed (SI Figure SI9a-b). However, the increase of the temperature may activate non-radiative recombination paths to other centers from the conduction band, thus decreasing the rate at which electrons are replenished in the singly ionized Zn vacancies, and, consequently enhancing the relative intensity of the band centered ~ 2.15 eV (SI Figure SI9c-d). Similarly, if the excitation density is sufficiently high, electrons are continuously pumped from the V_{Zn}, increasing the chance of extracting the second electron after the first one has been excited. Zn vacancies are known to produce highly localized states in ZnO[39] which usually present a high electron-phonon coupling.[40] Emission centres with high electron-phonon couplings tend to show small temperature changes even at liquid He temperatures,[41] thus explaining the extreme stability of the lineshape of both bands even down to 4 K.

When the doped materials are investigated, we observed that doping causes a large increase in the overall luminescence intensity of one order of magnitude. Figure 9 shows a comparison of the normalized PL spectra at low (4 K) and room temperature of the three different Zn_7InMO_{10} samples (M=In, Ga, Al), recorded with an excitation wavelength of λ_{ex}=315 nm. At 4 K, a significant blue shift of the emission maxima is visible, with its maximum located at $x_{m,4K}$(In)=1.75 eV, $x_{m,4K}$(Ga)=1.79 eV and $x_{m,4K}$(Al)=1.84 eV. However, at RT the shift of the emission maxima becomes almost negligible, and instead an asymmetric broadening at the high energy tail is observed for the doped oxides. This suggests the presence of at least two contributions to the spectra of the Al and Ga samples, the V_{Zn} band centered at $x_{c,1}$ ~ 1.74 eV, and a second contribution at higher energy, which seems to be influenced by the M^{3+} cation. In order to confirm the presence of this second contribution, RT PL spectra at different excitation densities were obtained, confirming the presence of a second band at 2.25 and 2.29 eV for Ga and Al-doped samples, respectively (SI Figures SI7b-c).This band can be related to transitions form neutral to singly ionized zinc vacancies ($V_{Zn}^{x} \rightarrow V'_{Zn}$), as in the undoped case. However, it alone cannot explain the low temperature behavior and spectra lineshape of the doped samples. Thus a third new band, characteristic only of the doped samples, has to be considered in order to fit the spectrum of both Ga and Al materials.

Peak	In^{3+}	Ga^{3+}	Al^{3+}	Proposed origin
1	1.73 eV	1.74 eV	1.75 eV	$V'_{Zn} \rightarrow V''_{Zn}$
2	2.15 eV	2.22 eV	2.28 eV	$V^{x}_{Zn} \rightarrow V'_{Zn}$
3	-	1.82 eV	1.87 eV	Related to Ga^{3+}/Al^{3+} in tetrahedral coordination

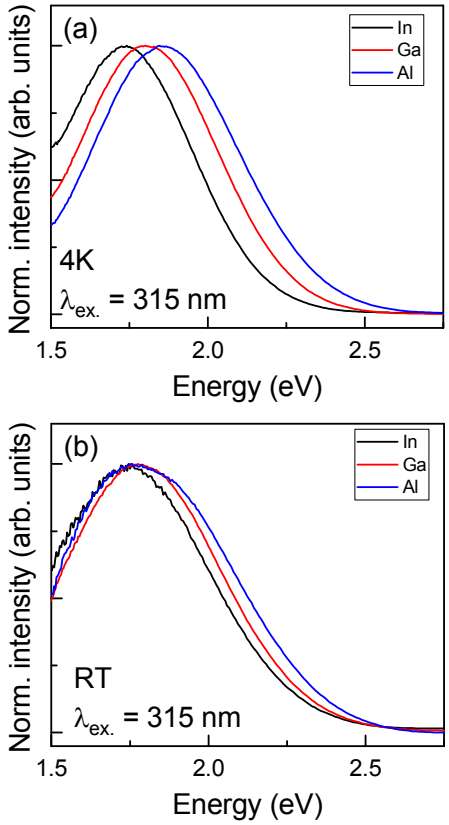

Figure 9. Normalized PL spectra of the three Zn_7InMO_{10} samples (M = In, Ga, Al) recorded with an excitation wavelength of λ_{ex} = 315 nm at (a) 4 K and (b) RT.

Figure 10 shows the resulting fit of the PL emission of both doped samples recorded at different temperatures to three proposed components (which are summarized in Table IV). The third band is centered at 1.82 and 1.87 eV for the Ga and Al doped oxides, respectively. As can be observed, at low temperature the luminescence spectra are dominated by this new third component, overcoming the intensity of the V_{Zn} band. At room temperature, on the other hand, both the third component and the V_{Zn} band contribute significantly to the PL, especially in the case of the Al doped compound, causing the observed broadening. These data were confirmed with the evaluation of the PL response at different excitation wavelengths (SI Figure SI8). In this sense, the UD sample whose spectra is dominated by the V_{Zn} emission, shows an emission maximum at λ_{ex} ~ 265 nm at any temperature, while the Ga-doped sample shows an emission maximum at λ_{ex} ~ 350 nm, irrespective of the temperature, for which the third band at 1.82 eV dominates at all temperatures. The Al-doped sample, on the other hand, shows an emission maximum at λ_{ex}=330 nm only at low temperature, where the third band dominates. However, at room temperature, which presents a similar contribution from both the first and the third bands (at 1.74 and 1.87 eV, respectively), the emission maximum are at an intermediate wavelength λ_{ex}=295 nm. The huge decrease in relative intensity of the V_{Zn} band in favor to the third component at low temperature suggests the existence of a competitive process between both bands, especially in Al doped materials. The origin of the third component is still unclear, however, it seems closely related the different atomic arrangement/coordination environment of Ga and Al compared to the UD sample.

Table IV: Energy peak center of the three components identified in the PL spectra at 4 K for each of the Zn_7InMO_{10} samples, with M=In, Ga, Al, and their proposed origin.

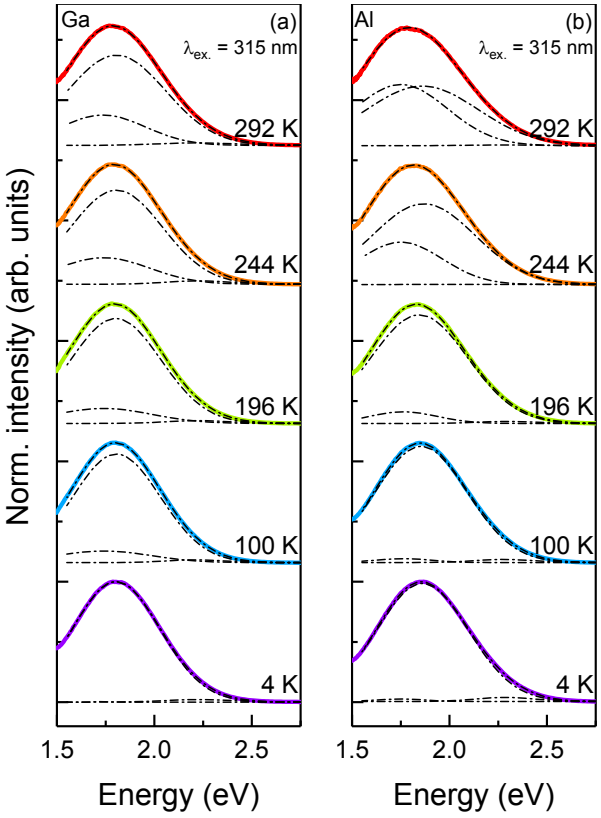

Figure 10. PL spectra of Zn_7InGaO_{10} (a) and Zn_7InAlO_{10} (b) recorded at different temperatures from 4 K up to RT.

Fitting to the three proposed components is shown for each spectrum in black dash-dotted lines.

The slight energy shift observed in the V_{Zn} energy levels could be explained in terms of the strain introduced by the different ionic radii of M^{3+}. On one hand, In^{3+} at bipyramidal sites, has larger ionic radius than Zn^{2+}, and therefore it should tend to expand the lattice when is incorporated to the wurtzite structure.[33] However, Ga^{3+} has close ionic radius to Zn^{2+}, while Al^{3+} presents lower ionic radius, all being at tetrahedral coordination. Therefore, the lattice should be almost undistorted or contracted, respectively, when these cations are present. This assumption is supported by the average metal-oxygen bonding distances obtained by DFT being 2.10 Å for InO_5, 1.96 Å for ZnO_4, 1.89 Å for GaO_4 and 1.83 Å for AlO_4. On the other hand, the nearest neighboring ions surrounding a vacancy tend relax outwards as the charge state of the vacancy changes from neutral (q= 0), to singly (q= -1), and to doubly (q= -2) ionized, resulting in the expansion of the lattice.[39,42] Therefore, the distortion originated by the cationic vacancies together with the one generated by the different M^{3+} ions, should modify the overall energy of the system.

For the UD sample, both, the effect of In^{3+} and vacancies contribute by expanding the lattice. This makes the ionized vacancies of the UD oxide less energetically preferred when compared to Al^{3+}-doped samples, in which the contractive distortion could almost cancel the expansion created by the vacancy. In the case of Ga^{3+}, the almost negligible lattice distortion makes the expansion of the vacancy the only contribution to tune of the vacancy energy level. Taking this into account, for the UD material, some of the energy released in the de-excitation process should be invested to increase the overall strain of the lattice, thus reducing the luminescence energy.[37,42] However, for Ga^{3+} and Al^{3+}doped samples, with smaller and almost negligible expansion, respectively, on the global effect in the lattice-distortion, would result into an increase of the luminescence energy.

CONCLUSIONS

On the basis of these results, we have shown by combining local and bulk diffractometric and spectroscopic techniques, that the luminescent behavior of Zn_7InMO_{10} (M=In, Ga, Al)) varies when the location and the oxygen coordination of the M^{3+} dopant changes, promoting microstructural variations in order to release the total energy of the structure of these semiconductor oxides as confirmed by DFT calculations. Despite the structural similarity between the different Zn_kInMO_{k+3} doped oxides, fundamental changes on the atomic arrangement take place upon substitution of In^{3+} atoms by Ga^{3+} or Al^{3+} with substantial modifications on their physical properties, as exemplified by the luminescence study reported here. DFT calculations have confirmed the preferential flat location of Ga^{3+} and Al^{3+} at the center of the wurtzite block, probing EDS mapping as a powerful and robust local technique for studying selective distribution of cations at the wurtzite-type lattice. Such information combined with XRD and NMR spectroscopy has provided a complete structural description of Zn_kInMO_{k+3} semiconductors that would contribute to the better control of their response, not only related with light emission applications, but also with their different uses as transparent electrodes or thermoelectric materials.

ASSOCIATED CONTENT

Supporting Information

XRD patterns of $Zn_7In_{2-X}M_XO_{10}$ (M=Ga, Al) with x=0-1.0, HRTEM images along the [010] and $[1\bar{1}0]$ zone axes for Zn_7InMO_{10} (M=Ga, Al), STEM-HAADF and ABF characterization of Zn_7InGaO_{10} along [010], origin of the Al^{3+} tetrahedral doublet and schematic representation of Zn_7InAlO_{10}, DFT calculations, normalized RT PL spectra with different excitation densities, PL spectra of Zn_7InMO_{10} (M=In, Ga, Al) as a function of the excitation wavelength, schematic of the different processes involved in the luminescence of the IZO materials. This material is available free of charge via the Internet at http://pubs.acs.org.

AUTHOR INFORMATION

Corresponding Author

Email: jgcalbet@ucm.es
Email: jrcastel@ucm.es

ACKNOWLEDGMENT

This work was supported by the Spanish Ministry of Innovation, Science and Technology and Spanish Ministry of Economy through Research Projects MAT2014-54372-R, MAT2017-82252-R, RTI2018-097195-B-I00 and PCIN-2017-106. This work is partially supported by ShanghaiTech ChEM under the grant number EM02161943. We thank the National Facility ELECMI ICTS and CAI for Nuclear Magnetic Resonance (UCM) and X-Ray Diffraction (UCM) for facilities. JB and ATP acknowledge financial support from the Comunidad de Madrid through the Talento fellowship 2017-T2/IND-5617 and PR65/19 Research Project, respectively.

REFERENCES

(1) Yu, X.; Marks, T. J; Facchetti, A. Metal oxides for optoelectronic applications. *Nat. Mater.* **2016**, 15, 383–396.

(2) Moriga, T.; Edwards, D. D.; Mason, T. O.; Palmer, G. B.; Poeppelmeier, K. R.; Schindler, J. L.; Kannewurf, C. R.; Nakabayashi, I. Phase relationships and physical properties of homologous compounds in the zinc oxide-indium oxide system. *J. Am. Ceram. Soc.* **1998**, 81(5), 1310–1316.

(3) Ohta, H.; Seo, W.-S.; K, Koumoto, K. Thermoelectric Properties of Homologous Compounds in the ZnO–In_2O_3 System. *J. Am. Ceram. Soc.* **1996**, 79, 2193–2196.

(4) García-Fernández, J.; Bartolomé, J.; Torres-Pardo, A.; Peche-Herrero, A.; Moreno, J.; Ramírez-Castellanos, J.; Cremades, A.; González-Calbet, J.M.; Piqueras, J. Structural characterization at the atomic level and optical properties

of the $Zn_kIn_2O_{k+3}$ ($3 \leq k \leq 13$) system. *J. Mater. Chem. C*. **2017**, 5, 10176.

(5) Lv, M.; Liu, G.; Xu, X. Homologous Compounds $Zn_nIn_2O_{3+n}$ (n = 4, 5, and 7) Containing Laminated Functional Groups as Efficient Photocatalysts for Hydrogen Production. *ACS Appl. Mater. Interfaces*. **2016**, 8(42), 28700–28708.

(6) Yoshinari, A.; Ishida, K.; Murai, K.; Moriga, T. Crystal and electronic band structures of homologous compounds $Zn_kIn_2O_{k+3}$ by Rietveld analysis and first-principle calculation. *Mater. Res. Bull*. **2009**, 44, 432–436.

(7) Li, C.; Bando, Y.; Nakamura, M.; Kimizuka, N. A modulated structure of $In_2O_3(ZnO)_m$ as revealed by high-resolution electron microscopy. *J. Electron Microscy*. **1997**, 46, 119–127

(8) Shannon, R. D.; Prewitt, C. T. Effective ionic radii and crystal chemistry. *J. Inorg. Nucl. Chem*. **1970**, 32 (5), 1427.

(9) Schmid, H.; Okunishi, E.; Oikawa, T.; Mader, W. Structural and elemental analysis of iron and indium doped zinc oxide by spectroscopic imaging in Cs-corrected STEM. *Micron*. **2012**, 43, 49–56.

(10) Schmid, H.; Okunishi, E.; Mader, W. Defect structures in ZnO studied by high-resolution structural and spectroscopic imaging. *Ultramicroscopy*. **2013**, 127, 76–84.

(11) Li, C.; Bando, Y.; Nakamura, M.; Kimizuka, N. High-resolution electron microscopy of a modulated structure in $InMO_3(ZnO)_m$ (M = In, Fe, Ga, and Al; m = integer): effect of solid solution formation. *Zeitschrift für Kristallographie*. **1999**, 214, 528–533.

(12) Li, C.; Bando, Y.; Nakamura, M.; Onoda, M.; Kimizuka, N. Modulated structures of homologous compounds $InMO_3(ZnO)_m$ (M= In, Ga; m= Integer) described by four-dimensional superspace group. *J. Solid State Chem*. **1998**, 139, 347–355.

(13) Li, C.; Bando, Y.; Nakamura, M.; Kimizuka, N. Relation between In ion ordering and crystal structure variation in homologous compounds $InMO_3(ZnO)m$ (M= Al and In; m= integer). *Micron*. **2000**, 31, 543–550.

(14) Yan, Y.; Da Silva, J. L. F.; Wei, S.-H.; Al-Jassim, M. Atomic structure of In_2O_3- ZnO systems. *Appl. Phys. Lett*. **2007**, 90, 261904.

(15) Da Silva, J. L. F.; Yan, Y.; Wei, S.-H. Rules of Structure Formation for the Homologous $InMO_3(ZnO)_n$ Compounds. *Phys. Rev. Lett*. **2008**, 100, 255501.

(16) Goldstein, A. P.; Andrews, S. C.; Berger, R. F.; Radmilovic, V. R.; Neaton, J. B.; Yang, P. Zigzag inversion domain boundaries in indium zinc oxide-based nanowires: structure and formation. *ACS Nano*. **2013**, 7(12), 10747–10751.

(17) Keller, I.; Mader, W. The Crystal Structure of $InGaO_3(ZnO)_4$: A Single Crystal X-ray and Electron Diffraction Study. *Z. Anorg. Allg. Chem*. **2010**, 636, 1045–104.

(18) Narendranath, S. B.; Yadav, A. K.; Ajithkumar, T. G.; Bhattacharyya, D.; Jha, S. N.; Dey, K, K.; Raja, T.; R. Nandini Devi, R. Investigations into variations in local cationic environment in layered oxide series $InGaO_3(ZnO)_m$ (m= 1–4). *Dalton Trans*. **2014**, 43, 2120.

(19) Nomura, K.; Kamiya, T.; Ohta, H.; Ueda, K.; Hirano, M.; Hosono, H. Carrier transport in transparent oxide semiconductor with intrinsic structural randomness probed using single-crystalline $InGaO_3(ZnO)_5$ films. *Appl. Phys. Lett*. **2004**, 85, 1993.

(20) Préaud, S.; Byl, C.; Brisset, F.; Berardan, D. SPS-assisted synthesis of $InGaO_3(ZnO)_m$ ceramics, and influence of m on the band gap and the thermal conductivity. *J. Am. Ceram. Soc*, **2020**, 103, 5, 3030-3038.

(21) Andrews, S. C.; Fardy, M. A.; Moore, M. C.; Aloni, S.; Zhang, M.; Radmilovic, V.; Yang, P. Atomic-level control of the thermoelectric properties in polytypoid nanowires. *Chem. Sci*. **2011**, 2, 706–714.

(22) Lou, Z.; Li, L.; Shen, G. $InGaO_3(ZnO)$ Superlattice Nanowires for High-Performance Ultraviolet Photodetectors. *Adv. Electron. Mater*. **2015**, 1, 1500054.

(23) Li, F.; Meng, Y.; Dong, R.; Yip, S. P.; Lan, C.; Kang, X.; Wang, F.; Chan, K. S.; Ho, J.C. High-Performance Transparent Ultraviolet Photodetectors Based on InGaZnO Superlattice Nanowire Arrays. *ACS Nano*, **2019**, 13, 12042–12051.

(24) Košir, M.; Čeh, M.; Ow-Yang, C. W.; Guilmeau, E.; Bernik, S. Structural features and thermoelectric properties of Al-doped $(ZnO)_5In_2O_3$ homologous phases. *J. Am. Ceram. Soc*. **2017**, 100, 3712–3721.

(25) Li, D. P.; Wang, G. Z.; Yang, Q. H.; Xie, X. J. Synthesis and Photoluminescence of $InGaO_3(ZnO)_m$ Nanowires with Perfect Superlattice Structure. *Phys. Chem. C*. **2009**, 113, 52, 21512-21515.

(26) Huang, D. L.; Wu, L. L.; Zhang, X. T.; Size-Dependent $InAlO_3(ZnO)_m$ Nanowires with a Perfect Superlattice Structure. *J. Phys. Chem. C*. **2010**, 114, 27, 11783-11786.

(27) Moriga, T.; Ishida, K.; Yamamoto, K.; Yoshinari, A.; Murai, K.-I. Structural analysis of homologous series of $Zn_kIn_2O_{k+3}$ (k=3, 5, 7) and Zn_kInGaO_{k+3} (k=1, 3, 5) as thermoelectric materials. *Mater. Res. Innovations*. **2009**, 13, 348-351.

(28) Dovesi, R.; Erba, A.; Orlando, R.; Zicovich-Wilson, C. M.; Civalleri, B.; Maschio, L.; Rérat, M.; S Casassa, S.; Baima, J.; Salustro, S.; Kirtman, B. Quantum-mechanical condensed matter simulations with CRYSTAL.*WIREs Comput. Sci*. **2018**, 8, e1360.

(29) Causa, M.; Dovesi, R.; Roetti, C. Pseudopotential Hartree-Fock study of seventeen III-V and IV-IV semiconductors. *Phys. Rev. B*. **1991**, 43, 11937-11943.

(30) Martinez-Casado, R.; Mallia, G.; M Harrison, N. M.; Pérez, R. First-Principles Study of the Water Adsorption on Anatase (101) as a Function □□ □□□ □□□□r□□□□ *J. Phys. Chem. C*□ □□□□□ 122□ 2□□3□□2□□□□□

(31) Martinez-Casado, R.; Todorović, M.; Mallia, G.; Harrison, N. M.; Pérez, R. First Principles Calculations on the Stoichiometric and Defective (101) Anatase Surface and

Upon Hydrogen and H2Pc Adsorption: The Influence of Electronic Exchange and Correlation and of Basis Set Approximations. Front. Chem. 2019, 7, 220.

(32) Yu, W.; Houben, L.; Tillmann, K.; Mader, W. Phase Contrast and HAADF Imaging of Structures in In_2O_3- ZnO Compounds in Cs-Corrected Electron Microscopes. *Microscopy and Microanalysis*. **2007**, 13, 28-29.

(33) Yu, W.; Mader, W. Displacement field measurement of metal sub-lattice in inversion domains of indium-doped zinc oxide. *Ultramicroscopy*. **2010**, 110, 411–417.

(34) Ash, J. T.; Grandinetti, P. J. Solid-state NMR characterization of ^{69}Ga and ^{71}Ga in crystalline solids. *Mag. Reson. Chem*. **2006**, 44, 823–831.

(35) Paul, G.; Bisio, C.; Braschi, I.; Cossi, M.; Gatti, G.; Gianotti, E.; Marchese, L. Combined solid-state NMR, FT-IR and computational studies on layered and porous materials. *Chem. Soc. Rev*. **2018**, 47, 5684-5739.

(36) Hopper, E. M.; Peng, H.; Hawks, S. A.; Freeman, A. J.; Mason, T. O. Defect mechanisms in the $In_2O_3(ZnO)_k$ system (k = 3, 5, 7, 9). *J. Applied Physics*. **2012**, 112, 093712.

(37) Peng, H.; Song, J.-H.; Hopper, E. M.; Zhu, Q.; Mason, T. O.; Freeman, A. J. Possible n–type carrier sources in $In_2O_3(ZnO)_k$. *Chem. Mater*. **2012**, 24, 1, 106-114.

(38) Bartolomé, J.; Maestre, D.; Cremades, A.; Amatti, M.; Piqueras, J. Composition-dependent electronic properties of indium–zinc–oxide elongated microstructures. *Acta Mater*. **2013**, 61, 1932–1943.

(39) Lyons, J. L.; Varley, J. B.; Steiauf, D.; Janotti, A.; Van de Walle, C. G. First-principles characterization of native-defect-related optical transitions in ZnO. *J. Appl. Phys*. **2017**, 122, 035704.

(40) Atta-Fynn, R.; Biswas, P.; Drabold, D. A. Electron–phonon coupling is large for localized states. *Phys. Rev. B*. **2004**, 69, 245204.

(41) Rebane, K. K. Impurity Spectra of Solids: Elementary Theory of Vibrational Structure, Plenum Press, New York, 1970.

(42) Janotti, A.; Van de Walle, C. G. Native point defects in ZnO. *Phys. Rev. B*. **2007**, 76, 165202.

For Table of Contents Only